Neutron and x-ray scattering studies of structural phase transitions and soft modes in Rb_2ZnBr_4

1998 J. Phys.: Condens. Matter 10 5861

(http://iopscience.iop.org/0953-8984/10/26/014)

J. Phys.: Condens. Matter **10** (1998) 5861–5874. Printed in the UK PII: S0953-8984(98)89546-5

Neutron and x-ray scattering studies of structural phase transitions and soft modes in Rb_2ZnBr_4

H Shigematsu†‖, H Mashiyama‡, Y Oohara§ and K Ohshima†

† Institute of Applied Physics, University of Tsukuba, Tsukuba 305-3573, Japan

‡ Department of Physics, Faculty of Science, Yamaguchi University, Yamaguchi 753-8512, Japan

§ Institute for Solid State Physics, University of Tokyo, Roppongi, Tokyo 106-8666, Japan

Received 24 November 1997, in final form 19 March 1998

Abstract. The low-temperature phase transitions of rubidium tetrabromozincate have been investigated with the use of neutron and x-ray scattering techniques to clarify the mechanism of the transitions and to determine the space groups of the low-temperature phases. The low-frequency excitations which soften at the phase transition at $T_3 = 112$ K have been measured by the inelastic neutron scattering technique. On the other hand, no soft phonon mode which makes a contribution to the phase IV–phase V transition at $T_4 = 76$ K has been observed. For both phase IV and phase V, superlattice reflections appear at the position $\frac{h}{2}\frac{k}{2}\frac{l}{3}$, where the Miller indices h, k, and l are referred to the lattice constants of phase I. In phase V, new Bragg reflections emerge at the position $hk0$: $h+k = 2n+1$ and increase in intensity continuously with decreasing temperature. The space groups are considered to be $P11b$ with $Z = 24$ for phase IV and $C1c1$ with $Z = 48$ for phase V on the basis of general group theoretical considerations. Furthermore, structural models for phase IV are proposed, to explain the extra extinction rule, the antiferroelectricity, and other observed characteristics of the crystal.

1. Introduction

Rubidium tetrabromozincate, Rb_2ZnBr_4, belongs to a family of A_2BX_4-type ferroelectrics with the β-K_2SO_4-type structure, like Rb_2ZnCl_4 [1]. The normal phase (phase I) has an orthorhombic structure (space group: $Pmcn$; $Z = 4$), where the c-axis is a pseudo-hexagonal axis, and $b \simeq \sqrt{3}a$. As the temperature decreases, the crystal transforms into an incommensurate phase (phase II) at $T_i = 347$ K [2, 3]. In phase II, the modulation wave vector is given by $q = (\frac{1}{3} - \delta)c_0^* \simeq \frac{5}{17}c_0^*$, where δ and c_0^* stand for the misfit parameter and the reciprocal-lattice parameter in the normal phase, respectively. The wave vector is almost independent of temperature except very close to the lock-in transition point ($T_C = 187$ K) [4, 5], below which the structure is commensurate with the wave vector $q = c_0^*/3$. Phase III shows ferroelectricity along the a-direction (space group: $P2_1cn$; $Z = 12$), and the ferroelectricity persists down to 4 K [1, 6].

Many of the A_2BX_4-type ferroelectrics—for example, Rb_2ZnCl_4, K_2ZnCl_4, and K_2CoCl_4—undergo the same succession of phase transitions: phase I, phase II, phase III. At lower temperature, further phase transitions take place at 74 K (Rb_2ZnCl_4), 145 K (K_2ZnCl_4), and 142 K (K_2CoCl_4) [7]. For the lowest-temperature phase, the superlattice

‖ Present address: Department of Quantum Engineering, Graduate School of Engineering, Nagoya University, Nagoya 464-8603, Japan.

0953-8984/98/265861+14$19.50

reflections were observed at $\frac{h}{2}\frac{k}{2}\frac{l}{3}_{Pmcn}$, where the indices are referred to the unit cell of phase I, which is indicated by the subscript $Pmcn$. The superlattice phase is reported to have the space group $C1c1$ [8].

On the other hand, for Rb_2ZnBr_4 two phase transitions have been reported, at $T_3 = 112$ K and $T_4 = 76$ K, and slight dielectric anomalies were also observed at 56 and 10 K [6]. A soft Raman mode has been observed for the scattering orientation $b(cc)a$ below T_3 [9], and the phase transition at T_3 is considered to be displacive. In phase IV between T_3 and T_4, antiferroelectricity along the b-direction is reported, and the superlattice reflections were observed at $\frac{h}{2}\frac{k}{2}\frac{l}{3}_{Pmcn}$ below T_3, like for other A_2BX_4-type ferroelectrics [10]. In phase V below T_4, the ferroelectricity appears along both the a- and the c-directions [6]. The existence of monoclinic domains has been confirmed from the optical activity [11].

Furthermore, the appearance of Bragg reflections at the positions $hk0_{Pmcn}$: $h + k = 2n + 1$ has been reported for phase V [12]. But the difference between the reflection conditions for phases IV and V has not been recognized [10]. That is, the structural features of phases IV and V are not clearly characterized as yet. Several authors have predicted the following space groups for the low-temperature phases: $C1c1$ for phase IV, and $C1c1$ or $P1$ for phase V. However, the crystal structures have not been determined [10, 12–14].

As for phase IV, three possible space groups were proposed: monoclinic forms ($C1c1$ and $P11b$) and a triclinic one ($P1$) [15]. In contrast, it has been reported that the crystal symmetry of phase IV is orthorhombic, from the observation of the crystal habit [11, 16].

In order to clarify the mechanism of the transitions at T_3 and T_4 and the structures at low temperature, we have performed both neutron and x-ray scattering experiments. In section 2, the experimental procedures of the scattering studies are described in detail. The results of inelastic neutron and elastic x-ray scattering studies below room temperature are presented in section 3. The phase transitions and the structures at low temperature are discussed in the final section.

2. Experimental procedure

Single crystals of Rb_2ZnBr_4 were grown by a slow evaporation method from an aqueous solution at 308 K. Although the molar ratio of AX to BX_2 in the aqueous solution is usually 2:1 for the A_2BX_4-type ferroelectrics, there are some exceptions; e.g. $(NH_4)_2ZnCl_4$ [17] and $(NH_4)_2ZnBr_4$ [18], for which the ratio 1:1 rather than 2:1 is appropriate for getting single crystals. For Rb_2ZnBr_4, we made sure that the single crystals were grown from a solution with a ratio between 2:1 and 1:1. Furthermore, since experience had shown that high-quality and large single crystals could more easily be grown from a solution with a ratio 1:1 than one with a ratio 2:1, we used an aqueous solution with the ratio 1:1 for Rb_2ZnBr_4. It took about three months to obtain large single crystals. The crystals were transparent and showed cleavage along a plane perpendicular to the b-axis. The samples were annealed at 393 K in air for ten hours before the experiment, to reduce the influence of included water [21].

The triple-axis spectrometer C1-1 installed in the Guide Hall at the JRR-3M research reactor of the Japan Atomic Energy Research Institute (JAERI), Tokai, was used for the neutron scattering. A crystal with a volume of 6.9 cm^3 was mounted in an aluminium can which was set in a closed-cycle He refrigerator (CTI). The sample temperature was controlled within 0.1 K by a TEMCON-IV system developed by Y Noda of Chiba University, Japan. Energy scans to observe the phonon spectra were carried out with a fixed incident neutron wavenumber of $k_i = 1.55$ $Å^{-1}$, with a pyrolytic graphite monochromator and an analyser. A beryllium filter was used in order to cut off higher-order reflections, and

an open–open–80′–80′ beam collimation was employed. The full width at half-maximum (FWHM) of the Bragg peaks found by the ω-scan method was 0.4°. The instrumental energy resolution was typically 0.2 meV (FWHM) for a constant-Q scan.

In the inelastic scattering experiments, the data were collected in the (a^*, b^*) scattering plane. Phonon dispersion curves were measured along the lines $(2+\xi\ 2-\xi\ 0)_{Pmcn}$: $\xi < 0.5$ and $(1-\xi\ 4+\xi\ 0)_{Pmcn}$: $\xi \geqslant 0.5$. On the former line, the reflection 220_{Pmcn} was strong, and an acoustic branch was observed. On the latter line, no acoustic branch was observed because the 050_{Pmcn} reflection is absent by an extinction rule for phase III [19, 20]. For both lines, it was mainly transverse components that were detected, because the phonon propagation vector was nearly perpendicular to the scattering vector. It should be noted that the reflections $\frac{5}{2}\frac{3}{2}0_{Pmcn}$ and $\frac{1}{2}\frac{9}{2}0_{Pmcn}$ were strong superlattice reflections below T_3. The lattice parameters were determined as $a = 7.63$ Å and $b = 13.30$ Å at 250 K from the peak positions of 200_{Pmcn} and 040_{Pmcn}.

The x-ray diffraction measurements were performed by using a four-circle diffractometer (Huber $422 + 511.1$) attached to a rotating-anode-type generator (Rigaku RU-300) with an x-ray power of 50 kV × 150 mA. Two different settings were used. First, for the measurements of the angles α, β, and γ, and the examination of whether or not an incommensurate phase exists in phase IV, the incident beam (Mo Kα_1 radiation) from a Mo target was monochromated by Ge111 with a good resolution. The Mo Kα_2 radiation was cut off by the knife edges of a divergent slit 0.2 mm in width and 0.2 mm in height. The FWHM of the Bragg reflections was less than 0.04° for this setting.

Second, for the investigation of the extinction rules and the measurements of the peak intensities, the incident beam (Mo Kα radiation) was monochromated by pyrolytic graphite (HOPG) to increase the reflection intensity. A collimator 0.8 mm in diameter was used to pass the incident beam.

Furthermore, we used an imaging-plate system installed at the Photon Factory (PF) of the National Laboratory for High Energy Physics, Tsukuba, in order to observe a wide region of reciprocal-lattice space.

The single-crystal specimens used in the experiment were cut to 1, 2, and 3 mm along the a-, b-, and c-axes, respectively, or to an almost spherical shape with a diameter of 0.25 mm. The sample was mounted on a copper sample holder, which was fixed on the cold head of a closed-cycle cryogenic refrigerator (Air Products, DE201), with the a-, b-, or c-axis as the rotation axis. The temperature of the sample was controlled within 0.1 K by the TEMCON-IV system.

3. Results

3.1. Neutron scattering

Figures 1 and 2 show the phonon dispersion curves in an extended-zone scheme along the $(\xi\ \xi\ 0)$ line, and a typical energy scan with constant Q within the optic mode region at 130 K, respectively. The observed phonon peaks were fitted to a double-Lorentzian-type cross-section convoluted with an instrumental resolution function. Two modes, which anticrossed each other at around $\xi \sim 0.7$, were observed. One is a transverse optic (TO) mode that is degenerate with a transverse acoustic (TA) branch at the zone-boundary S point ($\frac{1}{2}\frac{9}{2}0_{Pmcn}$; i.e. $\xi = 0.5$). Another is a TO branch whose frequency is higher than that of the degenerate TO mode at the same ξ-position. In figure 1, the solid curve for the degenerate

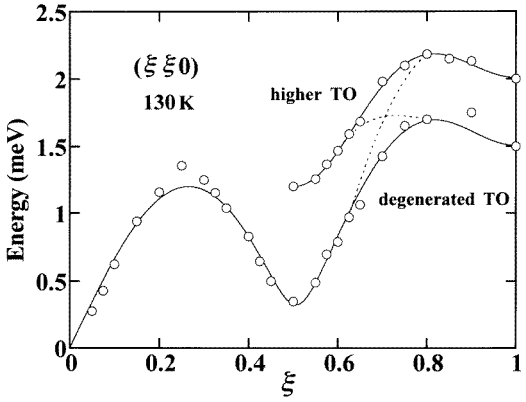

Figure 1. Phonon dispersion curves in an extended-zone scheme on the (ξ ξ 0) line at 130 K. The solid line for the degenerate TO mode shows the result of fitting equation (1) to the data. On the other hand, the solid line for the higher TO branch is just a guide to the eye.

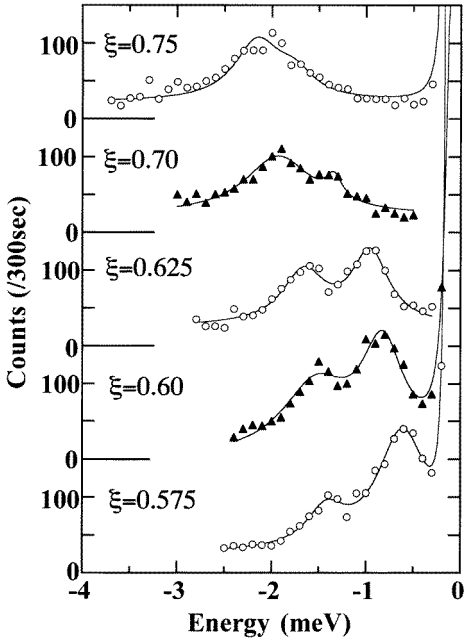

Figure 2. Energy scans with constant Q within the optic mode region at 130 K. They correspond to $\xi = 0.575$, 0.60, 0.625, 0.70, and 0.75 in figure 1.

TO mode is obtained by means of least-squares fitting to a Fourier decomposition:

$$E(\xi)^2 = \sum_{n=1}^{5} F_n [1 - \cos(n\pi\xi)] \tag{1}$$

like the dispersion relation of the Λ_2 and Λ_3 branches in the extended scheme for K_2SeO_4 [22]. The coefficients F_n correspond to the generalized effective interlayer force constants for coupling layers in the crystal separated by a distance of $nb/2$. The values of F_n for $n = 1$ to 5 are determined as 0.98(6), $-0.52(4)$, 0.25(5), 0.70(4), and $-0.10(4)$ meV^2 at 130 K.

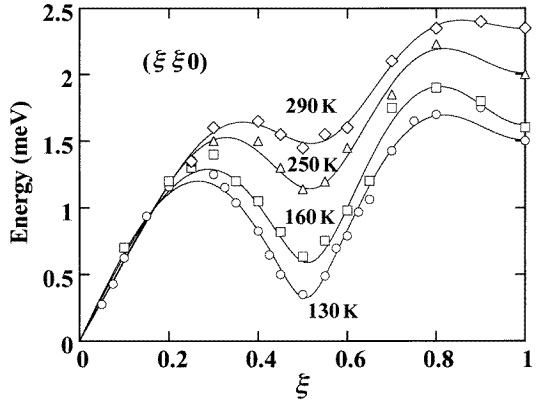

Figure 3. Phonon dispersion curves of the degenerate TO mode in an extended-zone scheme on the (ξ ξ 0) line at 290, 250, 160, and 130 K.

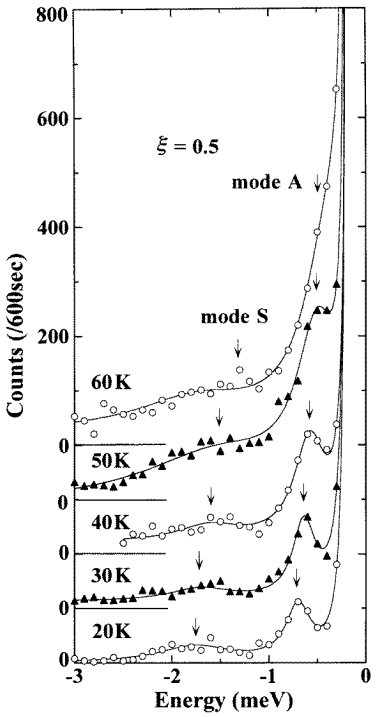

Figure 4. Energy scans with constant Q at $\frac{1}{2}\frac{9}{2}0_{Pmcn}$ below T_4. The excitation peaks of the soft modes A and S are indicated by arrows.

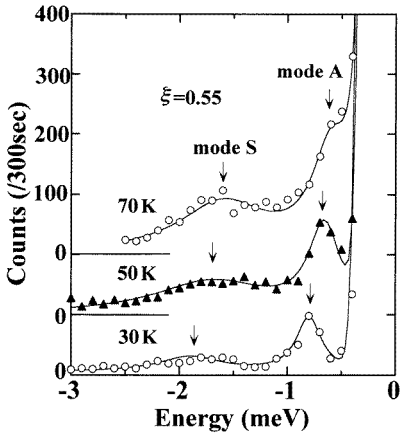

Figure 5. Energy scans with constant Q at $\xi = 0.55$ below T_4. The excitation peaks of the soft modes A and S are indicated by arrows.

On the other hand, the solid line for the higher TO branch is just a guide to the eye. Figure 3 shows the phonon dispersion curves of the degenerate TO mode at four temperatures above T_3. The solid lines were fitted using equation (1). The values obtained for F_n for $n = 1$ to 5 are 1.29(7), $-0.47(5)$, 0.25(5), 0.82(5), and $-0.22(5)$ meV^2 at 160 K, 1.90(7), $-0.29(5)$, 0.42(6), 0.76(5), and $-0.30(5)$ meV^2 at 250 K, and 2.48(5), $-0.25(4)$, 0.57(5), 0.53(5), and

$-0.29(5)$ meV^2 at 290 K. The force constant for nearest-neighbour layers, F_1, decreases sharply with decreasing temperature. The force constant F_4 is larger than F_2 and F_3, with the exception of the value at 290 K, and increases slightly with decreasing temperature. It is clear that this mode softens in the vicinity of the S point with decreasing temperature.

The temperature dependences of the energy scans with constant Q below T_4 at the S point and at $\xi = 0.55$ are shown in figure 4 and figure 5. Two temperature-dependent modes are clearly observed. The higher-energy mode (soft mode S) is identified as the soft mode reported by Francke *et al* [9]. The lower-energy mode (soft mode A) is a new one observed for the first time in this neutron scattering study.

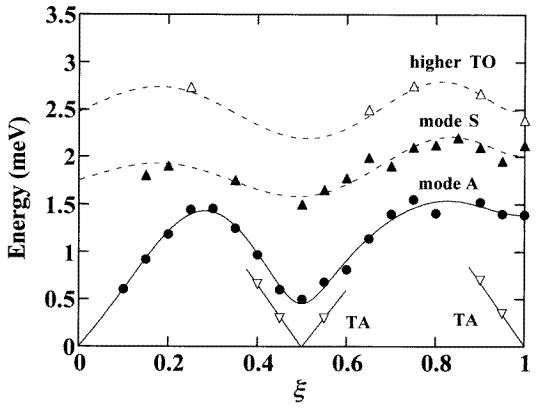

Figure 6. Phonon dispersion curves in an extended-zone scheme on the (ξ ξ 0) line at 50 K.

The peak intensity of the soft mode S is weaker than that of the soft mode A around the S point. By using the higher-resolution setting with the open–open–40′–40′ beam collimation, we have ascertained that the soft mode A persists to around T_4 where the mode does not soften, and therefore does not contribute to the phase IV–phase V transition. The dispersion relation at 50 K is shown in figure 6, as an example, for the low-temperature phase V. In the vicinity of $\xi = 0.5$ and 1, TA branches are observed clearly because the S point ($\xi = 0.5$) becomes equivalent to a Γ point, and the reflections $\frac{1}{2}\frac{9}{2}0_{Pmcn}$ and 050_{Pmcn} become Bragg reflections below T_3 and T_4, respectively. In the figure, the solid line for the soft mode A is obtained by a fitting to equation (1). The other two lines for the degenerate TO and higher TO modes are drawn as a guide to the eye. Although it may be reasonable to expect the TA mode to interact with the mode A, the TA branch becomes so broad and weak away from $\xi = 0.5$ or 1 that it was difficult to confirm the anticrossing. In figure 6, the clearly observed peak was regarded as mode A.

Figure 7 shows the temperature dependence of the observed mode frequencies at the S point; the solid curves are fitted according to the following relations:

$$E = C(T - T_3)^{0.5} \qquad \text{for the degenerate TO mode above } T_3 \tag{2}$$

$$E = C(T_3 - T)^{0.5} \qquad \text{for the soft mode S below } T_3 \tag{3}$$

$$E = C(T_3 - T)^{B} \qquad \text{for the soft mode A below } T_3. \tag{4}$$

The values of C are obtained as 0.099, 0.181, and 0.015 meV K$^{-1/2}$ for equations (2) to (4). In equation (4), B is used as a fitting parameter instead of 0.5, and the value obtained by the least-squares fitting was 0.84. It is clear that the degenerate TO mode and the soft modes S and A make a contribution to the phase III–phase IV transition.

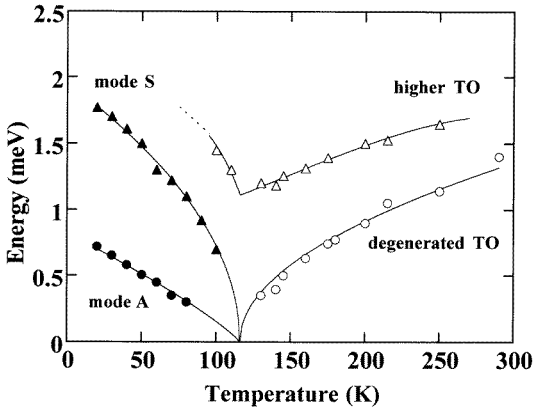

Figure 7. The temperature dependence of the observed mode frequencies at the S point.

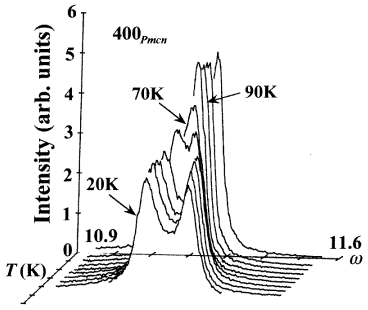

Figure 8. The ω-scan profiles of the 400_{Pmcn} reflection with the b-axis as the rotating axis. They were measured at 120 K, and at 100 K to 10 K in 10 K intervals.

On the other hand, the higher TO mode shows a weak softening as the temperature approaches T_3 from above, and does not vanish, but hardens with further decreasing temperature. Below 100 K, it was difficult to determine the peak position accurately, because the intensity became very weak with decreasing temperature.

3.2. X-ray scattering

Figure 8 shows the ω-scan profiles of the 400_{Pmcn} reflection with the b-axis as the rotating axis below T_3. A splitting of the Bragg reflection took place below T_4, and the separation increased continuously with decreasing temperature. Since the $0k0_{Pmcn}$ and $00l_{Pmcn}$ Bragg reflections did not split, the splitting of the $h00_{Pmcn}$-type Bragg reflections exhibits the existence of a monoclinic twin in phase V. The temperature dependence of the deviation angle $\Delta\beta = \beta - 90^\circ$ on cooling is plotted in figure 9; $\Delta\beta$ is 0.055° at 20 K. The other angles, α and γ, were 90° within the experimental error for phases IV and V. Note that the peak splitting of the superlattice reflections $\frac{h}{2}\frac{k}{2}\frac{l}{3}_{Pmcn}$, which has been reported for K_2ZnCl_4 [23], was not observed for phase IV. Therefore the structure is a commensurate one.

In addition to the appearance of superlattice reflections below T_3, the Bragg reflections at the position $hk0_{Pmcn}$: $h + k = 2n + 1$ appeared at T_4 and increased in intensity with decreasing temperature [24]. The temperature dependence of the integrated intensities of the 410_{Pmcn} reflection on heating and on cooling is shown in figure 10. We could not

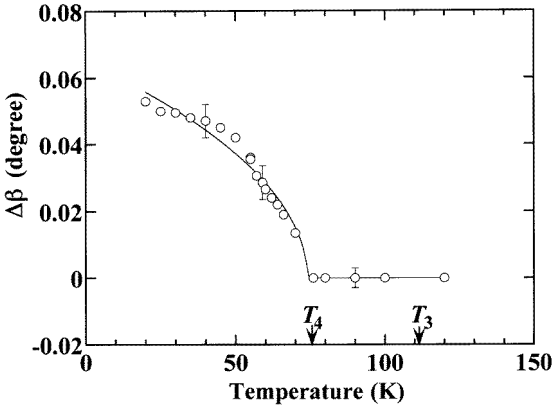

Figure 9. The temperature dependence of the deviation $\Delta\beta$ of the monoclinic angle from 90° on cooling.

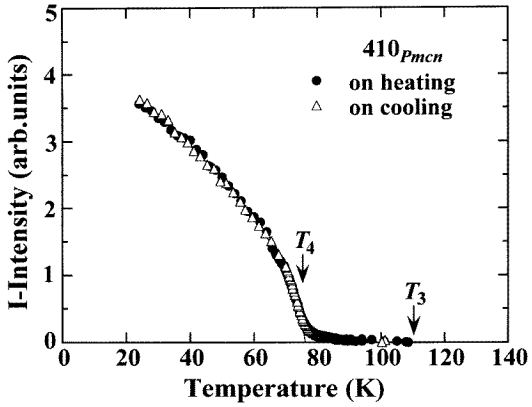

Figure 10. The temperature dependence of the integrated intensity of the 410_{Pmcn} Bragg reflection on heating and on cooling.

recognize any thermal hysteresis between heating and cooling processes. The temperature dependence of the integrated intensity I can be fitted to the following function:

$$I = A(T_4 - T)^{2\beta} \tag{5}$$

where A and T_4 denote the proportionality coefficient and the phase transition temperature, respectively. The values of T_4 and β are 75.84(8) K and 0.283(3) on heating, and 75.95(13) K and 0.281(4) on cooling, respectively.

Just above T_4, the peak intensity seemed to remain weak, but the width became a little larger, although the peak was not so broad as the diffuse scattering which can be observed at the phase III–phase IV transition at the superlattice reflection positions. We consider that the residual intensity in phase IV is caused by a local strain from the twinned structure of phase IV, and that the reflections with $hk0_{Pmcn}$: $h + k = 2n + 1$ are systematically absent for phase IV. The change of the extinction rules on going from phase IV to phase V was observed in this way. Both our results and those of others [6, 10, 12] are tabulated in table 1, where the Miller indices h_s, k_s, and l_s are referred to the $a_0 \times b_0 \times 3c_0$ superlattice cell of phase III and to the $2a_0 \times 2b_0 \times 3c_0$ one of phases IV and V. That is to say, the

Table 1. Crystal data for phases III, IV, and V of Rb_2ZnBr_4.

Transition temperature (K)	$T_4 = 76$	$T_3 = 112$	
Phase	V	IV	III
Space group	$C1c1$	$P11b$[a]	$P2_1cn$
Polar or antipolar	Ferroelectricity $\parallel \boldsymbol{a}$ Ferroelectricity $\parallel \boldsymbol{c}$	Ferroelectricity $\parallel \boldsymbol{a}$ Antiferroelectricity $\parallel \boldsymbol{b}$	Ferroelectricity $\parallel \boldsymbol{a}$
Extinction rules for systematic absence	h_s0l_s: $l_s = 2n+1$ $h_sk_sl_s$: $h_s + k_s = 2n+1$	h_s0l_s: $l_s = 2n+1$ $h_sk_sl_s$: $h_s + k_s = 2n+1$ h_sk_s0: $h_s + k_s = 4n+2$ and $h_s, k_s = 2n$	h_s0l_s: $l_s = 2n+1$ h_sk_s0: $h_s + k_s = 2n+1$
Angle (deg)	$\alpha = \gamma = 90$, $\beta \neq 90$	$\alpha = \beta = \gamma = 90$	$\alpha = \beta = \gamma = 90$
Cell dimension	$2a_0 \times 2b_0 \times 3c_0$	$2a_0 \times 2b_0 \times 3c_0$	$a_0 \times b_0 \times 3c_0$

[a] For the basis defined by equation (7).

410_{Pmcn} reflection in figure 10 corresponds to the $820_{\text{phase V}}$ reflection for phase V.

As a result of using the imaging-plate system installed at PF, no other extra reflection was observed at any temperature. Furthermore, for phases III, IV, and V, the observed structure factors $|F(\pm h_s \pm k_s \pm l_s)|$ assumed almost equal magnitudes within experimental errors. The observed diffraction patterns had the symmetry D_{2h} of the orthorhombic system.

4. Discussion

4.1. The behaviour of zone-boundary soft modes

By means of inelastic neutron scattering experiments investigating the low-temperature phase transitions at $T_3 = 112$ K and $T_4 = 76$ K, we have shown that the dispersion relations depend strongly on temperature, and that four low-energy phonon modes exist below room temperature. It is confirmed that three of them, the degenerate TO mode ($T > T_3$) and the soft modes S and A ($T < T_3$), make a contribution to the phase transition at T_3, because the frequencies of these modes tend to zero upon approaching T_3. On the other hand, the higher TO mode has no direct connection with III-to-IV or IV-to-V transition, and the frequency remains finite at the transition temperatures. Furthermore, an anticrossing behaviour of the degenerate TO mode and the higher TO mode is clearly observed from room temperature down to T_3. As a consequence of the temperature dependence of the force constants of the phonon dispersion curve of the degenerate TO mode, the softening results from the decrease of F_1, F_2, and F_3 in the presence of a strong and persistent force with a range $2b$ with magnitude F_4.

From group theoretical considerations, Dvorak and Kind [15] showed that three space groups, $P11b$, $C1c1$, and $P1$, are possible if the degenerate zone-boundary mode freezes in the A_2BX_4-type crystals. According to the theory, the mode splits into the totally symmetric mode S and the antisymmetric mode A. For Rb_2ZnBr_4, it is natural to consider that the higher-energy and the lower-energy modes can be attributed as modes S and A, respectively, because the soft mode S corresponds to the $b(cc)a$ Raman mode below T_3 [9]. It should be noted that the soft mode A has not been observed in Rb_2ZnCl_4 yet [8, 25]. The excitation energy of the soft mode A is so low that it could not be recognized under the energy resolution of the experiment. Although no hysteresis was observed in the integrated

intensity around T_4, as shown in figure 10, this transition should be of first order because the transition is accompanied by a latent heat release as found from the measurement of the heat capacity [26], and the spontaneous polarization along the *c*-axis changes discontinuously [6]. Furthermore, the integrated intensity has a steep temperature dependence, as the exponents obtained are 0.283(3) on heating and 0.281(4) on cooling. These values are smaller than the classical exponents $\beta = 0.5$ and $\beta = 0.35$, determined experimentally in previous investigations [8, 10]. So small an exponent may suggest that the transition is of first order.

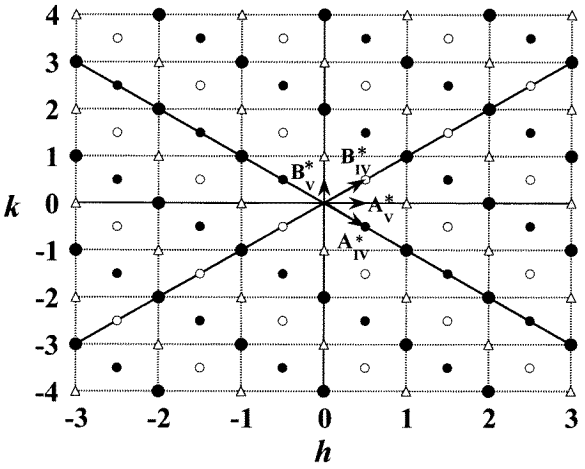

Figure 11. A schematic representation of the ($hk0$) reciprocal plane. Large full circles, small full circles and open circles, and open triangles indicate the existing positions of the Bragg reflections for phase III, the additional superlattice ones for phase IV, and the additional Bragg ones for phase V, respectively. Large full circles and small full circles indicate the positions of the reflections for the single-domain structure characterized by the reciprocal vectors $\boldsymbol{A}^*_{\mathrm{IV}}$, $\boldsymbol{B}^*_{\mathrm{IV}}$, and $\boldsymbol{C}^*_{\mathrm{IV}}$.

4.2. The structure of the low-temperature phases

As shown in table 1, we recognized differences between the reflection conditions for phases IV and V, which are schematically demonstrated in figure 11. Large full circles, small full circles and open circles, and open triangles indicate the existing positions of the Bragg reflections for phase III, the additional superlattice ones for phase IV, and the additional Bragg ones for phase V, respectively. $\boldsymbol{A}^*_{\mathrm{IV}}$, $\boldsymbol{B}^*_{\mathrm{IV}}$, $\boldsymbol{A}^*_{\mathrm{V}}$, and $\boldsymbol{B}^*_{\mathrm{V}}$ stand for the reciprocal-lattice vectors.

In phase IV, the following extinction rule for systematic absence was confirmed:

$$h_{\mathrm{s}}k_{\mathrm{s}}0\text{: } h_{\mathrm{s}} + k_{\mathrm{s}} = 4n + 2 \text{ and } h_{\mathrm{s}}, k_{\mathrm{s}} = 2n \tag{6}$$

for the $2a_0 \times 2b_0 \times 3c_0$ superlattice unit cell. Taking our results and other ones—for instance, dielectric measurements [1, 6] and results from space-group analysis [15]—into account, we assign the twin structure of space group $P11b$ with $Z = 24$ (referred to as model $\mathrm{IV_A}$ hereafter). This monoclinic structure is formed by unit-cell vectors related to that of the normal phase as follows:

$$\boldsymbol{A}_{\mathrm{IV}} = \boldsymbol{a}_0 - \boldsymbol{b}_0 \qquad \boldsymbol{B}_{\mathrm{IV}} = \boldsymbol{a}_0 + \boldsymbol{b}_0 \qquad \boldsymbol{C}_{\mathrm{IV}} = 3\boldsymbol{c}_0. \tag{7}$$

The proper symmetry operations of this phase are

$$[1]_{\mathrm{A}}\ x, y, z \qquad \text{and} \qquad [2]_{\mathrm{A}}\ x, y+\frac{1}{2}, \bar{z}+\frac{1}{2}. \tag{8}$$

Here the operation $[2]_{\mathrm{A}}$ corresponds to one of the n-glides of $P2_1cn$ for phase III. The reflections $h_{\mathrm{s}}k_{\mathrm{s}}0$: $h_{\mathrm{s}}+k_{\mathrm{s}}=4n+2$ or $h_{\mathrm{s}}+k_{\mathrm{s}}=2n+1$ are absent only in the single-domain model. If the structure of phase IV is considered as a twin structure with the domain ratio of 1:1, then the extinction rules obtained (except for $h_{\mathrm{s}}0l_{\mathrm{s}}$: $l_{\mathrm{s}}=2n+1$) as well as the existence of antiferroelectricity along the b-axis can be explained straightforwardly. In figure 11, large full circles and small full circles indicate the positions of the reflections for the single-domain structure characterized by the operations $[2]_{\mathrm{A}}$ and $[2]_{\mathrm{B}}$. Moreover, small open circles indicate the positions of the reflections for another twinned structure. Note that the reflections (large full circles) for the twinned structure overlap with those for the single-domain structure. In this twin model, it is not inevitable that the crystal system is orthorhombic. The three angles have values of 90° for the $2a_0 \times 2b_0 \times 3c_0$ unit cell, coincidentally.

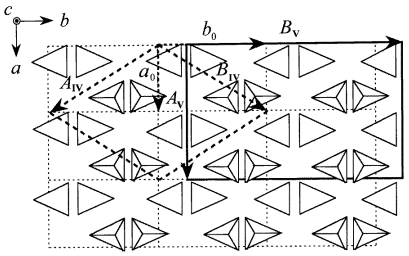

Figure 12. The projection of the structure between $z=0$ and $\frac{1}{3}$ along the c-axis for phases III, IV, and V. $ZnBr_4$ tetrahedra are indicated by triangles, and are set at the mean positions of the normal structure. All of the Rb ions are omitted for simplicity. The primitive unit cells for phases III, IV (models IV_A, IV_B, and IV_C), and V are denoted by dotted, dashed, and solid lines, respectively. The cell for model IV_D is the same cell as for phase V.

For phase V, the formation of a twin structure also occurs. In accordance with the crystal system (monoclinic) and the extinction rule, the space group should be $C1c1$ with $Z=48$, which permits spontaneous polarization within the a–c plane. This monoclinic structure is formed by the following superlattice cell vectors:

$$\boldsymbol{A}_{\mathrm{V}}=2\boldsymbol{a}_0 \qquad \boldsymbol{B}_{\mathrm{V}}=2\boldsymbol{b}_0 \qquad \boldsymbol{C}_{\mathrm{V}}=3\boldsymbol{c}_0. \tag{9}$$

A primitive cell can be defined for phase V by taking the unit cell of phase IV. Figure 12 shows a schematic picture of the structure projected along the c-axis between $z=0$ and $\frac{1}{3}$ for phases III, IV, and V [27]. In the figure, $ZnBr_4$ tetrahedra are indicated by triangles, and are set at the mean positions for the normal structure. All of the Rb ions are omitted for simplicity. The origin of phase V is translated to $\boldsymbol{b}_0/4$ with respect to that of phase IV [27]. The primitive unit cells in phases III, IV (model IV_A), and V are denoted by dotted, dashed, and solid lines, respectively.

Now we present other models for phase IV, which must naturally satisfy all of the extinction rules given in table 1 and the requirements of an orthorhombic system, as well as including the existence of antiferroelectricity along the b-axis. We consider additional symmetry operations on the basis of the groupoids [28, 29]. These structures (referred to as models IV_B, IV_C, and IV_D hereafter) are formed with the same unit cell, defined by relation (7) for models IV_B and IV_C and relation (9) for model IV_D. The symmetry

Table 2. Symmetry operations of the models IV_B, IV_C, and IV_D.

Model	Symmetry operations	
IV_B	$[1]_A$ x, y, z	$[2]_A$ $x, y+\frac{1}{2}, \bar{z}+\frac{1}{2}$
	$[3]_B$ $y+\frac{3}{4}, x+\frac{1}{4}, z+\frac{1}{2}$	$[4]_B$ $y+\frac{3}{4}, x+\frac{3}{4}, \bar{z}$
IV_C	$[1]_A$ x, y, z	$[2]_A$ $x, y+\frac{1}{2}, \bar{z}+\frac{1}{2}$
	$[3]_C$ $y+\frac{1}{4}, x+\frac{3}{4}, z+\frac{1}{2}$	$[4]_C$ $y+\frac{1}{4}, x+\frac{1}{4}, \bar{z}$
IV_D	$[1]_D$ x, y, z	$[2]_D$ $x+\frac{1}{2}, y+\frac{1}{2}, z$
	$[3]_D$ $x, \bar{y}, z+\frac{1}{2}$	$[4]_D$ $x+\frac{1}{2}, \bar{y}+\frac{1}{2}, z+\frac{1}{2}$
	$[5]_D$ $x+\frac{1}{4}, y+\frac{1}{4}, \bar{z}+\frac{1}{2}$	$[6]_D$ $x+\frac{3}{4}, y+\frac{3}{4}, \bar{z}+\frac{1}{2}$
	$[7]_D$ $x+\frac{1}{4}, \bar{y}+\frac{3}{4}, \bar{z}$	$[8]_D$ $x+\frac{3}{4}, \bar{y}+\frac{1}{4}, \bar{z}$

operations are given in table 2. The characteristics of phase IV can be explained on the basis of the partial remnants of these additional symmetries, $[3]_B$ and $[4]_B$ for model IV_B, $[3]_C$ and $[4]_C$ for model IV_C, and from $[5]_D$ to $[8]_D$ for model IV_D, which correspond to the symmetries of phase III. The structure of models IV_B and IV_C is based on the structure with space group $P11b$ for phase IV. The symmetry operations should contain the operations $[3]_B$ and $[4]_B$, or $[3]_C$ and $[4]_C$ in addition to the proper ones of (8). Pairs of operations $[1]_A$ and $[3]_B$, $[2]_A$ and $[4]_B$, $[1]_A$ and $[3]_C$, and $[1]_A$ and $[4]_C$ correspond to the c-glide operations of phase III. Then the crystal system becomes orthorhombic C_{2v}. The difference between model IV_A and models IV_B and IV_C lies in whether the extinction rule h_s0l_s: $l_s = 2n+1$ holds approximately (coincidentally) or exactly (inevitably). On the other hand, the structure of model IV_D is based on the structure with space group $C1c1$ for phase V. The sets of operations from $[1]_D$ to $[4]_D$ and from $[5]_D$ to $[8]_D$ correspond to those of the $C1c1$ structure. The relation between $[1]_D$ and $[5]_D$ is not a group element; however, it leads to the extra extinction rule of equation (6). The point group of the model IV_D is orthorhombic C_{2v}, which supports the x-ray scattering result and the assertion that phase IV has a dielectric nature.

The full reflection conditions and the relation for the magnitude with eight structure factors $|F(\pm h_s \pm k_s \pm l_s)|$ for phase IV are satisfied by considering a twin structure that is the same as the structure of model IV_A, IV_B, IV_C, or IV_D. If the domain ratio of the monoclinic twin is 1:1 in phases IV and V, then all eight structure factors $|F(\pm h_s \pm k_s \pm l_s)|$ have the same magnitude, and the observed symmetry D_{2h} of phase IV can be explained directly. When the domain ratio deviates from 1:1, the relationship of these structure factors changes as shown in table 3. Therefore, when the domain ratio is not equal to 1:1, the structure of phase IV can be that of model IV_A, IV_B, IV_C, or IV_D. In models IV_B and IV_C, the relationships of these structure factors are the same, and agreement between the observed and calculated structure factors for many reflections is required in order to determine which model is appropriate. However, according to the results of x-ray scattering investigations, the domain ratio is almost 1:1 within the experimental errors, and we could not definitely determine the structure of phase IV. Incidentally, it has been reported that the domain ratio of the $C1c1$ structure for K_2CoCl_4 was 1.014:0.986 [27].

As noted in section 4.1, the IV-to-V transition is a first-order one. Usually the space group changes at the transition. If this is the case, the space group of phase IV is $P11b$, since that of phase V is definitely $C1c1$. Model IV_B and model IV_C are both plausible for explaining the orthorhombic crystal system. In order to establish which model is actually the

Table 3. The relationship between the structure factors and indices for phases IV (models IV_A, IV_B, IV_C, and IV_D) and V when the domain ratio deviates from 1:1. The Miller indices are referred to the $2a_0 \times 2b_0 \times 3c_0$ cell.

Phase IV	Model IV_A $P11b$	$\lvert F(h_s k_s l_s)\rvert = \lvert F(\overline{h_s} k_s l_s)\rvert = \lvert F(h_s \overline{k_s} \overline{l_s})\rvert = \lvert F(\overline{h_s} k_s \overline{l_s})\rvert$, $\lvert F(h_s \overline{k_s} l_s)\rvert = \lvert F(\overline{h_s} k_s l_s)\rvert = \lvert F(h_s \overline{k_s} \overline{l_s})\rvert = \lvert F(\overline{h_s} k_s \overline{l_s})\rvert$	
	Models IV_B and IV_C $P11b$ based	$\lvert F(h_s k_s l_s)\rvert = \lvert F(\overline{h_s} k_s l_s)\rvert = \lvert F(h_s \overline{k_s} \overline{l_s})\rvert = \lvert F(\overline{h_s} k_s \overline{l_s})\rvert$ $= \lvert F(h_s \overline{k_s} l_s)\rvert = \lvert F(\overline{h_s} k_s l_s)\rvert = \lvert F(h_s k_s \overline{l_s})\rvert = \lvert F(\overline{h_s} k_s \overline{l_s})\rvert$	Main reflections
		$\lvert F(h_s k_s l_s)\rvert = \lvert F(\overline{h_s} k_s \overline{l_s})\rvert = \lvert F(h_s k_s \overline{l_s})\rvert = \lvert F(\overline{h_s} k_s l_s)\rvert$, $\lvert F(h_s \overline{k_s} l_s)\rvert = \lvert F(\overline{h_s} k_s l_s)\rvert = \lvert F(h_s \overline{k_s} \overline{l_s})\rvert = \lvert F(\overline{h_s} k_s \overline{l_s})\rvert$	Superlattice reflections
	Model IV_D $C1c1$ based	$\lvert F(h_s k_s l_s)\rvert = \lvert F(\overline{h_s} k_s \overline{l_s})\rvert = \lvert F(h_s k_s \overline{l_s})\rvert = \lvert F(\overline{h_s} k_s l_s)\rvert$ $= \lvert F(h_s \overline{k_s} l_s)\rvert = \lvert F(\overline{h_s} k_s l_s)\rvert = \lvert F(h_s \overline{k_s} \overline{l_s})\rvert = \lvert F(\overline{h_s} k_s \overline{l_s})\rvert$	Main reflections
		$\lvert F(h_s k_s l_s)\rvert = \lvert F(h_s \overline{k_s} l_s)\rvert = \lvert F(\overline{h_s} k_s \overline{l_s})\rvert = \lvert F(\overline{h_s} \overline{k_s} l_s)\rvert$, $\lvert F(h_s k_s \overline{l_s})\rvert = \lvert F(\overline{h_s} \overline{k_s} l_s)\rvert = \lvert F(\overline{h_s} k_s l_s)\rvert = \lvert F(h_s \overline{k_s} \overline{l_s})\rvert$	Superlattice reflections
Phase V	$C1c1$	$\lvert F(h_s k_s l_s)\rvert = \lvert F(h_s \overline{k_s} l_s)\rvert = \lvert F(\overline{h_s} k_s \overline{l_s})\rvert = \lvert F(\overline{h_s} \overline{k_s} l_s)\rvert$, $\lvert F(h_s k_s \overline{l_s})\rvert = \lvert F(h_s \overline{k_s} \overline{l_s})\rvert = \lvert F(\overline{h_s} k_s l_s)\rvert = \lvert F(h_s \overline{k_s} l_s)\rvert$	

most appropriate representation of phase IV, it is desirable to collect scattering intensities very carefully, and to refine the crystal structure very accurately.

Acknowledgments

One of the authors (HS) would like to thank Dr A Yamamoto of the National Institute for Research in Inorganic Materials for helpful discussions, and Professor Y Noda of Chiba University for fruitful discussions and technical support in the neutron and x-ray scattering experiments.

References

[1] Sawada S, Shiroishi Y, Yamamoto A, Takashige M and Matsuo M 1977 *J. Phys. Soc. Japan* **43** 2101
[2] De Pater C J and Van Dijk C 1978 *Phys. Rev.* B **18** 1281
[3] De Pater C J, Axe J D and Currat R 1979 *Phys. Rev.* B **19** 4684
[4] Gesi K and Iizumi M 1978 *J. Phys. Soc. Japan* **45** 1777
[5] Iizumi M and Gesi K 1983 *J. Phys. Soc. Japan* **52** 2526
[6] Yamaguchi T and Sawada S 1991 *J. Phys. Soc. Japan* **60** 3162
[7] Cummins H Z 1990 *Phys. Rep.* **185** 211
[8] Mashiyama H, Sugimoto K, Oohara Y and Yoshizawa H 1992 *J. Phys. Soc. Japan* **61** 3042
[9] Francke E, Le Postollec M, Mathieu J P and Poulet H 1980 *Solid State Commun.* **35** 183
[10] Kasano H, Shigematsu H, Mashiyama H, Iwata Y, Kasatani H and Terauchi H 1994 *J. Phys. Soc. Japan* **63** 1681
[11] Meekes H and Janner A 1988 *Phys. Rev.* B **38** 8075
[12] Ueda T, Iida S and Terauchi H 1982 *J. Phys. Soc. Japan* **51** 3953
[13] Hogervorst A C R and Helmholdt R B 1988 *Acta Crystallogr.* B **44** 120
[14] Belobrova I A, Aleksandrova I P and Moskalev A K 1981 *Phys. Status Solidi* a **66** K17
[15] Dvorak V and Kind R 1981 *Phys. Status Solidi* b **107** K109
[16] Hogervorst A C R and Helmholdt R B 1988 *Acta Crystallogr.* B **44** 120
[17] Meerburg P A 1903 *Z. Anorg. Chem.* **37** 199
[18] Shigematsu H, Kasano H and Mashiyama H 1993 *J. Phys. Soc. Japan* **62** 3929
[19] Quilichini M, Dvorak V and Boutrouille 1991 *J. Physique* I **1** 1321

[20] Mashiyama H, Sugimoto K, Oohara Y and Yoshizawa H 1992 *J. Phys. Soc. Japan* **61** 3042
[21] Takai S, Atake T and Gesi K 1993 *J. Phys. Chem. Solids* **54** 213
[22] Iizumi M, Axe J D, Shirane G and Shimaoka K 1977 *Phys. Rev.* B **15** 4392
[23] Gesi K 1992 *J. Phys. Soc. Japan* **61** 1225
[24] Shigematsu H, Mashiyama H, Oohara Y and Ohshima K 1996 *Physica* B **219+220** 611
[25] Wada M, Sawada A and Ishibashi Y 1981 *J. Phys. Soc. Japan* **50** 531
[26] Nomoto K, Atake T, Chaudhuri B K and Chihara H 1983 *J. Phys. Soc. Japan* **52** 3475
[27] Mashiyama H 1991 *J. Phys. Soc. Japan* **60** 180
[28] Yamamoto A and Ishihara K N 1988 *Acta Crystallogr.* A **44** 707
[29] Perez-Mato J M and Iglesias J E 1977 *Acta Crystallogr.* A **33** 466